Applied Energy 235 (2019) 1468–1475

Contents lists available at ScienceDirect

Applied Energy

journal homepage: www.elsevier.com/locate/apenergy

4D *in situ* synchrotron X-ray tomographic microscopy and laser-based heating study of oil shale pyrolysis

Tarik Saif[a], Qingyang Lin[a,*], Ying Gao[a], Yousef Al-Khulaifi[a], Federica Marone[b], David Hollis[c], Martin J. Blunt[a], Branko Bijeljic[a]

[a] Department of Earth Science and Engineering, Imperial College London, London SW7 2AZ, UK
[b] Swiss Light Source, Paul Scherrer Institut, CH-5232 Villigen, Switzerland
[c] LaVisionUK Ltd, Grove Technology Park, Grove, Oxfordshire OX12 9FF, UK

HIGHLIGHTS

- Green River oil shale pyrolysis was characterized using 4-D synchrotron imaging.
- Laser-based heating was combined with X-ray synchrotron imaging at the micron-scale.
- Digital Volume Correlation was used to generate 3-D full-field strain maps.
- First micro-fractures were observed at 354 °C followed by rapid pore space expansion.
- Fracture development in oil shale depends on the dynamics of the local strain field.

ARTICLE INFO

Keywords:
Oil shale
Pyrolysis
Fractures
Synchrotron
X-ray micro-tomography
Digital Volume Correlation

ABSTRACT

The comprehensive characterization and analysis of the evolution of micro-fracture networks in oil shales during pyrolysis is important to understand the complex petrophysical changes during hydrocarbon recovery. We used time-resolved X-ray microtomography to perform pore-scale dynamic imaging with a synchrotron light source to capture in 4-D (three-dimensional image + real time) the evolution of fracture initiation, growth, coalescence and closure. A laser-based heating system was used to pyrolyze a sample of Eocene Green River (Mahogany Zone) up to 600 °C with tomograms acquired every 30 s at 1.63 μm computed voxel size and analyzed using Digital Volume Correlation (DVC) for full 3-D strain and deformation maps. At 354 °C the first isolated micro-fractures were observed and by 378 °C, a connected fracture network was formed as the solid organic matter was transformed into volatile hydrocarbon components. With increasing temperature, we observed simultaneous pore space growth and coalescence as well as temporary closure of minor fractures caused by local compressive stresses. This indicates that the evolution of individual fractures not only depends on organic matter composition but also on the dynamic development of neighboring fractures. Our results demonstrate that combining synchrotron X-ray tomography, laser-based heating and DVC provides a powerful methodology for characterizing dynamics of multi-scale physical changes during oil shale pyrolysis to help optimize hydrocarbon recovery.

1. Introduction

As global conventional oil supplies begin to plateau, the energy industry is investing significantly to identify, probe, recover, and process oil and gas that was once unknown, or difficult to be accessed or recovered [1–3]. Oil shale is an unconventional energy resource with more than 600 known deposits [4,5]. The potential value of an oil shale deposit is predominantly dependent on its thickness, depth and organic content [4,6]. The Eocene Green River Formation represents the world's largest deposit with sedimentary structures spanning 65,000 km^2 across Wyoming, Colorado and Utah with an estimated oil reserves of 4.3 trillion barrels [4,7].

Oil shale is a fine-grained sedimentary rock consisting of organic matter that releases hydrocarbons (shale oil) and combustible gas during pyrolysis [5,8]. One key advantage of producing energy from oil shales over conventional fossil fuels is that it has relatively higher hydrogen to carbon atomic ratios and lower oxygen to carbon ratios [9]. The pyrolysis of oil shale refers to its thermal processing by anaerobic

* Corresponding author.
E-mail address: q.lin11@imperial.ac.uk (Q. Lin).

https://doi.org/10.1016/j.apenergy.2018.11.044
Received 18 July 2018; Received in revised form 10 November 2018; Accepted 12 November 2018

heating (300–600 °C) [10,11]. The first stage involves the heating of oil shale where heat transfer occurs from the heat carrier to the oil shale surface, and then from the surface to its interior. The endothermic energy barrier starts to be overcome at a temperature of approximately 300 °C, the temperature at which oil shale pyrolysis starts. The second stage is the pyrolysis of the organic matter which is thermally decomposed to produce shale oil vapor, non-condensable gases, pyrolysis water and a carbonaceous residue. The kerogen decomposition rate accelerates as the temperature increases. The third step involves diffusion and flow of shale oil vapor, non-condensable gas, and water vapor through an interconnected pore and fracture network. Oil shale pyrolysis involves complex reactions and its oil yield and quality is dependent on several factors including pyrolysis temperature [12,13], heating rate [13–15], heating duration [16,17], particle size [18,19] and mineral content [20,21].

During the pyrolysis of oil shale, several coupled physical and chemical phenomena occur concurrently, such as heat transfer, chemical reaction kinetics, multiphase flow, phase changes, and mineral alteration and interaction. These processes are highly coupled and interrelated; therefore, separating each phenomenon accurately is challenging. In this study, we performed an imaging-based characterization of the dynamics of the pore space development and evolution during oil shale pyrolysis, which acts as a porous medium for the storage and percolation of oil and gas after decomposing the organic matter. Further understanding, including visualizations and quantification, is crucial in providing valuable data sets to better model pyrolysis processes and ultimately enhance the development of applied oil shale utilization technologies.

Fig. 1 shows the imaging and characterization techniques used to quantify the fine-grained sedimentary structures. X-ray microtomography (micro-CT) is often used for the visualization and quantification of geological samples including the investigation of pore network properties, micro-textures, fractures and transport properties [22–24]. Micro-CT offers several advantages: samples can be evaluated in three-dimensions (3-D), non-destructively with minimal sample preparation, and high spatial resolution down to the micron level can

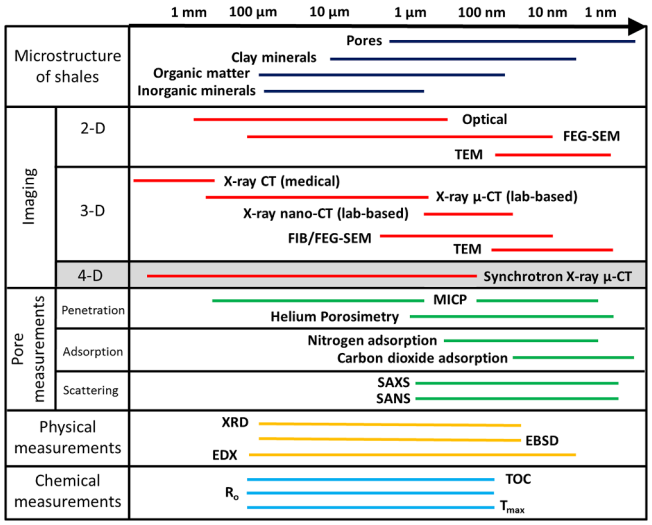

Fig. 1. Complementary imaging and analytical techniques can be used to characterize oil shale microstructures at varying scales. To capture the dynamic changes in pore structures and micro-fracture development during oil shale pyrolysis, a time resolved/fast imaging and *in situ* heating experiment is necessary.

be achieved. Oil shales have been characterized using micro-CT to capture the organic matter and inorganic minerals within the sample and to study pyrolysis. Tiwari et al. [25] reported the effect of temperatures from 350 to 500 °C on the pyrolysis process using imaging (42 µm voxel size) to characterize pores with an equivalent diameter of 500 µm across. Saif et al. [26] studied the microstructural development of the oil shale sample as the temperature increased from 300 to 500 °C with different voxel sizes (12 µm and 2 µm). Connected pore space was formed between temperatures of 400 °C and 500 °C along the kerogen-rich layers. In addition, Saif et al. [27] established a workflow to characterize fractures and rock mineral textures at different scales demonstrating both heterogeneity and anisotropy. Although useful in providing an initial insight into pore space development during pyrolysis, these static studies were limited as they only focused on the analysis of 3-D tomograms acquired from samples before and after pyrolysis. The spatially and temporally dependent pore evolution process could not be observed and quantified. To comprehensively capture these dynamics in oil shale pore-scale processes, it is necessary to have rapid acquisition times, high resolution and the integration of an *in situ* pyrolysis rig.

To unlock our understanding of dynamic processes, recent studies have concentrated on high resolution X-ray imaging at the pore scale using a synchrotron light source [28–30]. This can provide a powerful 4-D imaging tool that enables the visualization and quantification of pore-scale processes at high time resolution. Synchrotron radiation consists of a bright parallel beam of X-rays [31,32]. The high flux density (orders of magnitude higher than for conventional lab-based X-ray sources) reduces exposure times (order of 10 s per scan) to achieve dynamic imaging. Additional benefits of using synchrotron radiation include a simplified tomographic reconstruction algorithm due to the use of a parallel beam, and the tunability of the X-ray energy to a narrow energy band [33].

Recently, Saif et al. [34] dynamically captured the pore structure evolution for Green River (Mahogany Zone) oil shale, demonstrating the major benefit of rapid synchrotron imaging (with a voxel size of 2 µm) for studying oil shale pyrolysis. The first pore space was captured at 390 °C, followed by a rapid porosity increase between 390 °C and 400 °C forming an inter-connected pore structure. The scanning time resolution was 160 s; however, no 3-D strain mapping was performed. To comprehensively characterize pore structure and strain development during oil shale pyrolysis we require faster scanning times, improved spatial resolution and controlled localized heating. Combining 4-D imaging with Digital Volume Correlation (DVC) allows for the computation of 3-D full-field displacement and strain maps from volume images acquired during oil shale pyrolysis [35]. The data can be visualized and analyzed to quantify deformation-induced microstructural changes such as pore-growth and coalescence related to fracture development and would, therefore, improve our understanding of the dynamics of pore-space evolution during thermal decomposition.

In this study, we employed the TOMCAT beamline (Swiss Light Source) [36], with a diode laser-based heating system to investigate pore structure evolution during pyrolysis for the Green River oil shale. This was coupled with Digital Volume Correlation to relate fluctuations in displacement with changes in microstructure during oil shale deformation due to pyrolysis. The results provide a spatial resolution high enough (1.63 µm computed voxel size) and a temporal resolution fast enough (30 s per 3-D scan) to resolve both the physical transformation in the oil shale microstructure and the dynamics of micro-fracturing. A brief description of the experimental procedure used at the synchrotron light source, followed by an overview of the DVC technique, is presented first. The 3-D tomogram results are then analyzed in detail providing new insights into the preferential evolution of micro-fractures during pyrolysis and their subsequent coalescence creating a

connected fracture network.

This work has direct application for oil shale pyrolysis, since it quantifies the onset temperature for hydrocarbon production as well as the connectivity of the micro-fractures, which provide a flow pathway for recovery. More generally, the combination of fast micron-resolution imaging and analysis can be applied to other energy-related problems, including conventional oil and gas production, shale oil and gas, and *in operando* studies of fuel cells [37].

2. Materials and methods

The oil shale sample studied here was acquired from Mahogany zone of the Eocene lacustrine Green River Formation (Uinta Basin, Utah, USA). It represents a classic reference sedimentary rock for Type I kerogen with characteristic biomarkers including isoprenoid, steranes, and terpanes indicating organic matter predominantly from aquatic organisms comprising lacustrine planktonic algae [4,38]. The mineral composition of the sample is mainly dolomite, calcite, quartz, and feldspars with small amounts of illite, analcime and pyrite [26].

In preparation for the *in situ* dynamic experiment at TOMCAT, core samples (2.5 mm in diameter and 4 mm in length) were selected. The sample holder was made from hot-pressed boron nitride (thermal conductivity for BN is 15–50 W m K^{-1}, maximum working temperature is 2773 K/2500 °C), which is relatively X-ray transparent while being chemically and thermally stable (the thermal expansion for BN is 36×10^{-6} at 1273 K).

The experiment was performed at the TOMCAT beamline of the Swiss Light Source. A custom-built diode laser-based heating system was used to pyrolyze the oil shale samples at atmospheric pressure [39], see Fig. 2. The laser-based heating system incorporated two near-infrared (IR) diode lasers, operating at a wavelength of 980 nm. The oval spot for each laser is of 4 × 6 mm. The BN holder was then inserted into a stainless steel adaptor connected to an alumina rod that was secured to the rotation stage.

A monochromatic X-ray beam energy of 20 keV was used with the beam filtered by passing through 200 µm and 50 µm Aluminum filters (Fig. 2). The exposure time for projection was 30 ms and there were 1001 projections in total for each scan with a field of view of 4.16 mm × 3.51 mm. The acquisition time for each scan was 30 s with a computed voxel size of 1.63 µm. The oil shale sample was heated in a nitrogen environment from 20 °C to 600 °C at a heating rate of 10 °C/min between 20 and 300 °C and 1 °C/min between 300 and 600 °C (samples were cooled down after 600 °C) to acquire 3-D scans with increasing pyrolysis temperature.

Each tomogram was reconstructed using a re-gridding Fourier transform-based reconstruction algorithm [40], and processed and using the Avizo 9.0 program (FEI, Visualization Sciences Group, Thermo Fisher Scientific). In this study, within a reconstructed image, the darkest phase represents the pore space. A non-local means edge preserving filter [41] was applied to the 3-D images to reduce image noise followed by segmentation using Otsu's algorithm to extract the pore space for further analysis [34].

We applied Digital Volume Correlation (DVC), a technique providing displacements and strains measurements within a sequence of tomographic volume images. 3-D synchrotron images capturing oil shale pyrolysis with increasing temperature were imported in RAW format (a stack of gray-scale images) and deformation vectors based on the change of gray-scale structures were computed using the LaVision DaVis 8.4 program. For DVC processing at least two scans of the sample are required, typically a reference scan of the undeformed sample and a second scan of the sample in its deformed state. In this study, a series of image volumes featuring successive deformation steps were processed, capturing the time evolution of pore space while temperature increases.

The volume correlation in this study is computed using a cross-correlation method operating on the intensity values (i.e. contrast pattern) of volumetric images and is performed using a predictor-corrector approach with Fast Fourier Transform algorithm (FFT) predictor steps, and Direct Correlation refinement steps [42–44]. The

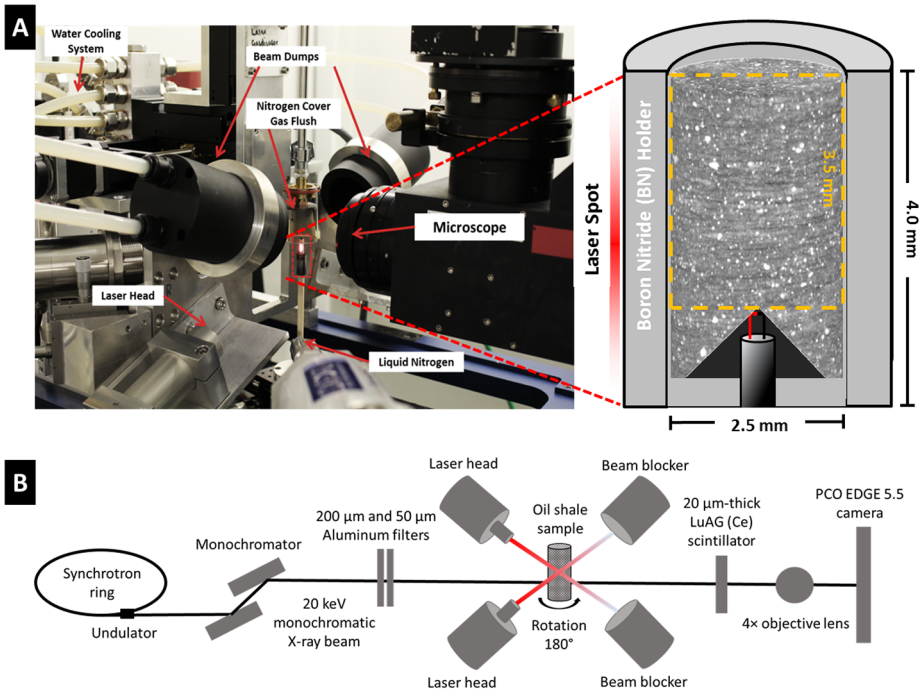

Fig. 2. (A) Experimental apparatus used at the TOMCAT beamline (X02DA), consisting of a diode laser-based system to heat an oil shale sample (2.5 mm diameter). (B) Schematic of the TOMCAT beam apparatus with the monochromatic X-ray beam transmitting through the laser-heated oil shale sample onto a scintillator, which is focused and imaged by the objective lens and a sCMOS camera array.

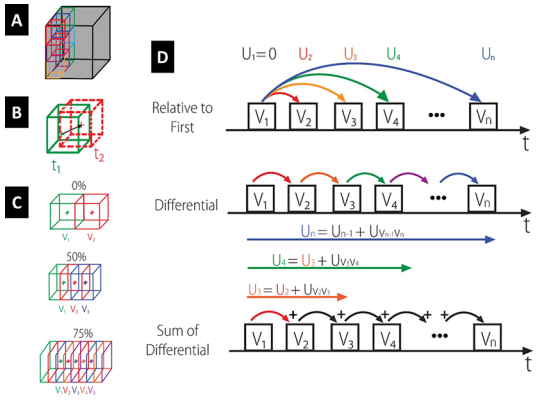

Fig. 3. Schematic illustrating the Digital Volume Correlation (DVC) method. (A) The measurement volume is divided into smaller sub-volumes. (B) For each sub-volume the new position in the deformed state (t_2) is obtained by correlation of the voxel contrast within the sub-volume. The vector connecting the subvolume centers of initial (t_1) and deformed state (t_2) is the associated displacement vector, (U). (C) Without overlap the sub-volumes are directly adjacent to each other. At 50% overlap there are three sub-volumes in the same space as the overlap-free configuration and at 75% overlap this corresponds to five sub-volumes in the same space. In this figure, only the overlapping along the x-direction is illustrated, but the actual overlap will be along all three coordinate axes. (D) Graphical representation of the correlation modes with the storage of a zero-vector field ($U_1 = 0$) for the first (reference) volume. All other results are aligned with the time step of the second volume of the corresponding correlation step, i.e. the vector field U_2 is aligned with volume V_2 and so on. Note that the first non-zero vector field U_2 is identical for all correlation modes. In relative to first mode, every volume is correlated with the first volume of the series which gives the best accuracy but the correlation may fail when relative changes between volumes become too large. In differential correlation mode, each volume is correlated to its predecessor, thus the resulting vector field only describes changes between subsequent volumes. In sum of differential mode, the differential vector fields are summed up to arrive at the total deformation with respect to the first volume, which is appropriate for the large deformations observed in this study.

measurement volume is divided into smaller sub-volumes with a dimension of N × N × N voxels and the shift of the contrast patterns within the sub-volumes is then tracked from reference to the deformed state (Fig. 3). Once the best matching position of a sub-volume in the deformed state is found, the associated shift is given by the vector connecting the sub-volume centers of initial and deformed state. Together, the vectors of all sub-volumes form 3D matrix of vectors representing local sample displacements. Local strain values are calculated by numerical derivation of the displacement vector field by the DVC software.

Given that this image correlation approach creates one vector per sub-volume, the spatial resolution of the resulting vector field is related to the sub-volume size. Smaller sub-volumes give better spatial resolution but also increase the noise due to loss of correlation statistics. When processing data, the aim is to find the optimum sub-volume size where the sub-volumes are small enough to capture the essential features of deformation while still large enough to give accurate vectors. In this study, the maximum correlation was performed which uses the gradient of the displacement from the previous pass to deform the sub-volume on the subsequent pass until the highest possible correlation and signal to noise ratio was reached. A final sub-volume of 48 × 48 × 48 voxels with a 75% overlap was used, where the overlap allows an increase in spatial density of vectors without a reduction of the sub-volume size. This provided a balance between noise and an adequate spatial resolution for strain in the pyrolyzed oil shale sample.

3. Results and discussion

Fig. 4 displays a 2-D cross-sectional area of the sample during heating. For oil shale, domains with the darkest gray levels (lowest counts) represent pore space with the lighter gray regions representing the organic matter, while the brighter gray levels reflect the solid matrix, and the brightest phase represents high density minerals such as pyrite.

It can be observed that there is no visible porosity change below 350 °C (Fig. 4A). Within the complex fine-grained microstructure, fractures at the micron level formed along the organic-rich layers were detected at 360 °C contributing a porosity of 3.6%. With an additional increase in temperature to 370 °C a negligible visible difference in micro-fracture growth is observed, despite sample porosity increasing to 5.7%. At 380 °C, a significant porosity increase was captured (porosity increased to 13.2%) as the micro-fractures propagate along the kerogen-rich bedding with the development of major and minor fractures within the sample. Further heating from 390 °C to 450 °C resulted in a smaller porosity increase from 20.2% to 20.9%. In Fig. 4B, the critical pore volume changes took place between 350 °C and 400 °C. The most significant change in oil shale pore volume was achieved at 378 °C. The alteration in oil shale porosity with heating primarily represents the loss of organic matter during thermal decomposition where immobile kerogen is transformed into mobile oil and gas. With increasing temperature, there is a build-up in the internal vapor pressure of isolated pores which exceeds the local mechanical strength and the matrix fractures.

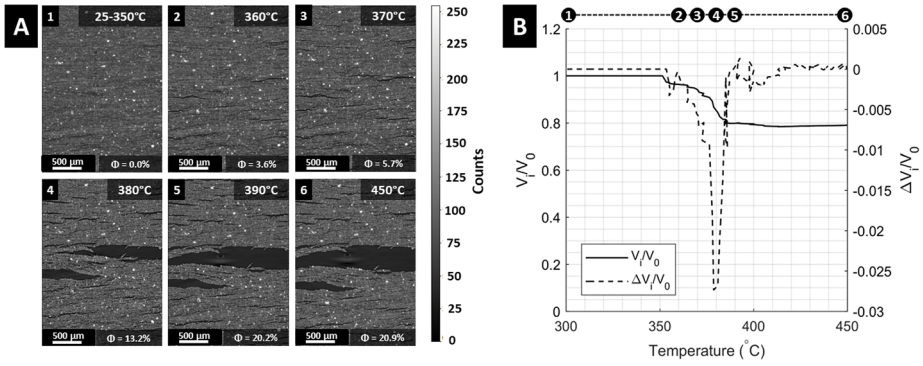

Fig. 4. (A) Two-dimensional cross-sections of three-dimensional images at different temperatures during pyrolysis showing the development of micro-fractures (dark). The acquisition time for each scan is 30 s and a voxel size of 1.63 µm under a laser-based heating system. (B) Plot showing the volume loss of the sample matrix excluding pore space (V_i) and the fractional matrix volume change (ΔV_i) for every 1 °C increase in temperature.

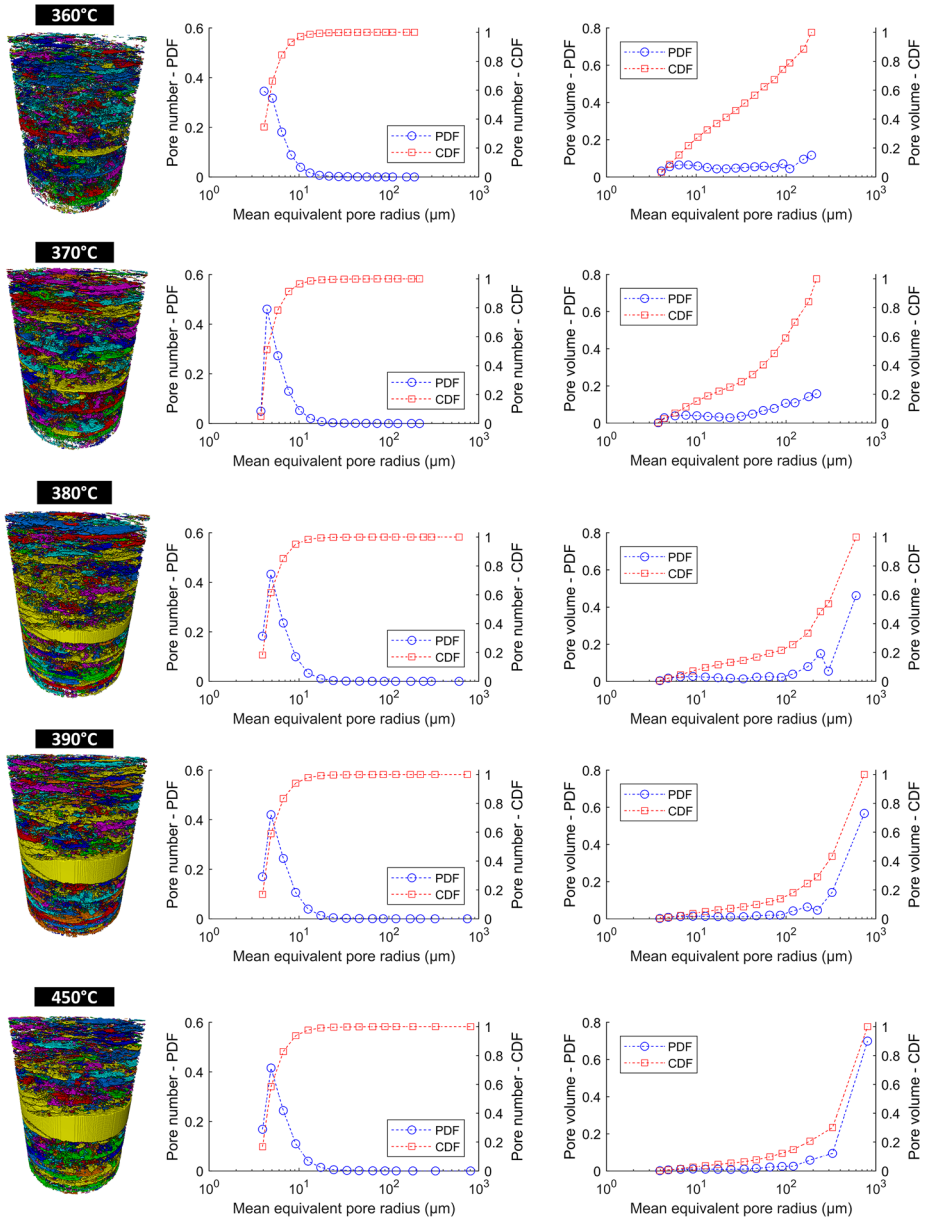

Fig. 5. Visualization of the pore space connectivity (each color represents a single connected region of the pore space). An increasingly well-connected pore space is formed, as micro-fractures propagate largely along the kerogen-rich laminations. The pore size distribution (both probability density function and cumulative distribution function) at 360 °C, 370 °C, 380 °C, 390 °C and 450 °C reveal that with increasing pyrolysis temperature there are modest changes where the smaller pores dominate in number while the larger pores have a greater volumetric contribution. (For interpretation of the references to color in this figure legend, the reader is referred to the web version of this article.)

Fig. 5 shows the visualization of the pore space for the sample at temperatures from 360 °C to 450 °C. Each interconnected portion of the pore space is indicated with a different color. At 360 °C, the majority of the pores were disconnected (indicated by the wide color range), whereas with increasing temperature, the pores and fractures along the organic-rich laminations becomes apparent particularly between 370 °C and 380 °C and the pore space is well connected. At each temperature, individual pores were divided into different size groups to create a pore size distribution (characterized by probability density functions and cumulative distribution functions), represented by a mean equivalent pore radius (Fig. 5).

As the temperature increases we see that the number of pores and their contribution to the total pore volume shifts to the very largest pore sizes. The results in Fig. 5 show initially the presence of several small pores developing during oil shale pyrolysis which then grow and coalesce into a smaller number of larger sized fractures which occupy the majority of the pores. At 360 °C and 370 °C we find that pores having an equivalent radius approximately between 4.1 μm and 6.4 μm, and 4.4 μm to 5.8 μm, respectively, dominate the distribution. At 360 °C, pores approximately ranging from 4.1 μm to 74.0 μm in equivalent radius occupy 67.3% of the total pore volume, with the remaining 32.7% pore volume occupied by pores having an equivalent radius approximately between 92.0 μm and 191.9 μm. At 370 °C, we observe a shift towards larger pores dominating the total pore volume with pores approximately ranging from 55.7 μm to 218.8 μm in equivalent radius having the greatest volumetric contribution, occupying 59.6% of the pore space. At 380 °C, pores with an equivalent radius between 3.9 μm and 12.6 μm comprise 98.4% of the total pore number while larger pores with a mean equivalent pore radius of 602 μm in the form of lateral micro-fractures occupy 46.2%. A further increase in pyrolysis temperature to 390 °C and 450 °C does not significantly change the size of the pores in terms of number of pores between 3.9 μm and 12.6 μm that continue to dominate the distribution. The main difference is observed in the dominant mean equivalent pore radius with 743.4 μm and 807.5 μm, representing large connected fractures, occupying the majority of the pore space at 390 °C and 450 °C respectively. The largest change in pore structure is observed between 360 °C and 380 °C, which provides further evidence of the importance of this temperature range.

DVC analysis allows us to identify and quantify successive

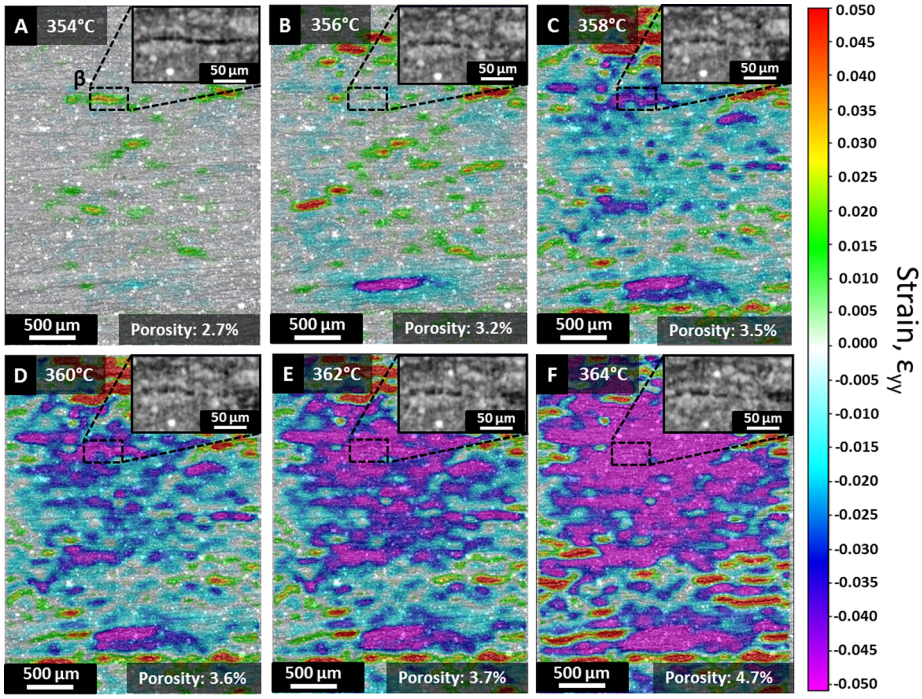

Fig. 6. Micro-fracture development during oil shale pyrolysis between 354 °C and 364 °C (A–F). Digital Volume Correlation (DVC) was used to quantify the strain within the oil shale sample during thermal maturation. We follow micro-fracture β (initial fracture shown in inset A) to examine its development with increasing pyrolysis temperature from 354 °C to 364 °C. ε_{yy} strain components are superimposed onto the associated gray-scale image revealing that with increasing pyrolysis temperature the local compressive stresses cause temporary closure of minor fractures.

deformation steps. Fig. 6 represents the full-field internal strain distribution measurements computed using DVC for the sample during pyrolysis. Note that although the term "strain" is used here, because the material is opening up to reveal pores, the strain maps do not represent the material strain, but instead the relative movement of material adjacent to pore opening sites. Maps of the strain in the vertical direction (ε_{yy}) were superimposed onto the associated gray-scale images. In this analysis, we follow micro-fracture β (initial fracture shown in Fig. 6A) to examine its development with increasing pyrolysis temperature from 354 °C to 364 °C. At 354 °C, the first micro-fracture was observed with strain values in the range of 1.2–3.3%. With an increase in temperature to 356 °C (Fig. 6B), the computed strain values associated with micro-fracture β decreased to 0.4–0.9% as the surrounding micro-fractures developed due to the thermal decomposition of organic matter and accompanying internal gas pressure build-up. As the pyrolysis temperature rose further to 358 °C, the micro-fracture β closed due to corresponding negative values of strain (compression) in the range of −1.5 to −4.2%. As the oil shale sample pyrolysis temperature increased to 364 °C (Fig. 6F), there was large compression surrounding micro-fracture β which resulted in a further closure of the fracture at strain values of −4.5 to −5.0%. This analysis has revealed the dynamic evolution of micro-fractures during oil shale pyrolysis, illustrating that with increasing temperature there is temporary closure of minor fractures due to local compressive stresses. Individual fractures not only depend on the content of hydrocarbons but also on the dynamic development of neighboring fractures.

Fig. 7 shows the DVC measurements of the spatial distribution of the

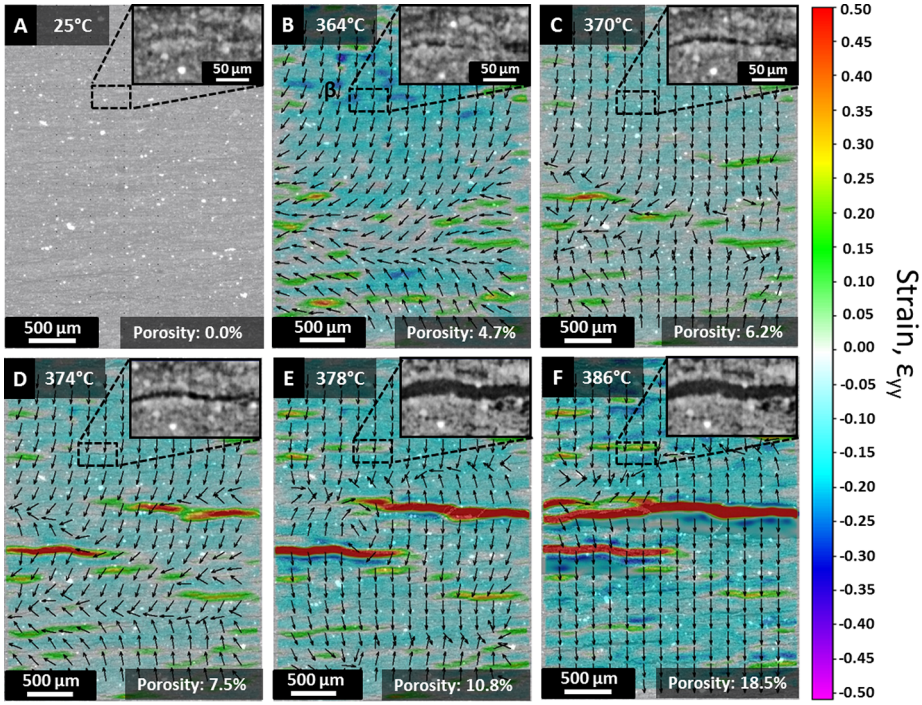

Fig. 7. The growth of minor and major fractures is observed between 364 °C and 386 °C (B–F). Digital Volume Correlation (DVC) quantifies the strain within the oil shale sample during thermal maturation. ε_{yy} strain components are superimposed onto the associated gray-scale image revealing initially a compressive force as indicated by the vector arrows, followed by expansion due to the build-up of internal pressure as solid organic matter is transformed into volatile components.

volumetric strain ε_{yy} along with vector arrows for the oil shale sample at pyrolysis temperatures of 364–386 °C. Between 364 °C and 370 °C the sample underwent slight compression coupled with the development of minor fractures with associated strain values of 5.4 – 36.5%. At 374 °C, major fractures formed laterally across the oil shale sample with high tensile strain values in the range of 28.2–46.4% (Fig. 7D). As the pyrolysis temperature rose further to 386 °C, the strain values associated with the major fractures increased further towards 50% (Fig. 7F). These results indicate that the oil shale pyrolysis process consists of compressive forces followed by expansion due to the build-up of internal pressure as solid organic matter is transformed into volatile components.

4. Discussion and conclusions

We have characterized the deformation of oil shale at elevated pyrolysis temperatures and the evolution of micro-fractures critical for determining hydrocarbon flow behavior. To achieve this, we imaged a sample of Green River (Mahogany zone) oil shale in 3-D using a time-resolved synchrotron X-ray source at 1.63 µm computed voxel size while being subjected to increasing pyrolysis temperature up to 600 °C using a laser-based heating system. Laser-based heating was used to pyrolyze oil shale at a heating rate of 1 °C/min to 600 °C with 3-D images captured every 30 s revealing internal structural development.

Three-dimensional full-field strain mapping and micro-fracture development were quantified by Digital Volume Correlation (DVC) during pyrolysis to evaluate oil shale deformation and fracturing. From the sequence of 3-D tomographic volume images, the deformation vectors based on the change of gray-scale structures were computed. The first micro-fractures were observed at 354 °C followed by rapid expansion up to 390 °C where the majority of the pore space became inter-connected. The results revealed anisotropic micro-fracture pyrolysis induced behavior with fractures opening perpendicular to the oil shale bedding followed by coalescence along laminated structures to generate a connected fracture network due to the build-up of internal pressure as solid organic matter was transformed into mobile components. Our study revealed the importance of capturing the dynamics of simultaneous fracture development and closure within the most important heating regime during pyrolysis. Simultaneous expansion and closure of fractures was observed to be dependent not only on the content of hydrocarbons but also on the dynamics of the local strain field. With these state-of-the-art imaging and novel analytical techniques, the visualization and quantification of successive deformation steps allow for advanced modeling of fluid flow during pyrolysis.

This work provides quantitative guidelines for the application of oil shale pyrolysis, showing how the connectivity of the micro-fracture network develops from around 350 °C. More generally, the same combination of rapid micron-resolution imaging and analysis could be applied to other energy systems that involve porous media, from oil-bearing rocks [45] to fuel cells, batteries and catalysts [37].

Acknowledgements

The authors acknowledge the Paul Scherrer Institut for provision of synchrotron radiation beamtime at the TOMCAT beamline X02DA. We would like to thank Gordan Mikuljan for his technical assistance. Many thanks to Alex Nila (LaVision, United Kingdom) for his support with Digital Volume Correlation. We are also grateful for financial support from the Imperial College Consortium on Pore-Scale Modelling and the Department of Earth Science and Engineering at Imperial College London.

References

[1] IEA. World energy outlook; 2015. Available: < http://www.worldenergyoutlook.org/weo2015/ > [accessed 10 January 2010].
[2] BP. Energy outlook to 2035; 2016. Available: < https://www.bp.com/content/dam/bp/pdf/energy-economics/energy-outlook-2016/bp-energy-outlook-2016.pdf > [accessed 10 January 2010].
[3] World Energy Council. World energy focus; 2017. < https://www.worldenergy.org/publications/2017/world-energy-focus-2017/ > [accessed April 14, 2018].
[4] Dyni JR. Geology and resources of some world oil-shale deposits. Oil Shale 2003;20:193–252.
[5] Speight JG. Origin and properties of oil shale; 2012. http://doi.org/10.1016/B978-0-12-401721-4.00001-1.
[6] Speight JG. The chemistry and technology of petroleum. CRC Press; 2014.
[7] Birdwell JE, Mercier TJ, Johnson RC, Brownfield ME. In-place oil shale resources examined by grade in the major basins of the Green River Formation, Colorado, Utah, and Wyoming. US Geol Surv Fact Sheet 2012;3145:2013.
[8] Lee S. Oil shale technology. CRC Press; 1990.
[9] Strizhakova Ya, Usova TV. Current trends in the pyrolysis of oil shale: a review. Solid Fuel Chem 2008;42:197–201. https://doi.org/10.3103/S0361521908040022.
[10] Gallin William, Day Roger L, Keiter Robert. Oil shale: a solution to the liquid fuel dilemma 2010;vol. 1032. https://doi.org/10.1021/bk-2010-1032.
[11] Lee S, Speight JG, Loyalka SK. Handbook of alternative fuel technologies. CRC Press; 2007.
[12] Chen M, Shi Y. Flash pyrolysis of Fushun oil shale fine particles in an experimental fluidized-bed reactor. Oil Shale 2010;27:297–308.
[13] Williams PT, Ahmad N. Influence of process conditions on the pyrolysis of Pakistani oil shales. Fuel 1999;78:653–62. https://doi.org/10.1016/S0016-2361(98)00190-2.
[14] Değirmenci L, Durusoy T. Effect of heating rate and particle size on the pyrolysis of Göynük oil shale. Energy Sources 2005;27:787–95.
[15] Nazzal JM. Influence of heating rate on the pyrolysis of Jordan oil shale. J Anal Appl Pyrolysis 2002;62:225–38.
[16] Williams PT, Chishti HM. Influence of residence time and catalyst regeneration on the pyrolysis–zeolite catalysis of oil shale. J Anal Appl Pyrolysis 2001;60:187–203.
[17] Solomon PR, Carangelo RM, Horn E. The effects of pyrolysis conditions on Israeli oil shale properties. Fuel 1986;65:650–62.
[18] Ahmad N, Williams PT. Influence of particle grain size on the yield and composition of products from the pyrolysis of oil shales. J Anal Appl Pyrolysis 1998;46:31–49.
[19] Khalil AM. Oil shale pyrolysis and effect of particle size on the composition of shale oil. Oil Shale 2013;30:136–46. https://doi.org/10.3176/oil.2013.2.04.
[20] Espitalie J, Madec M, Tissot B. Role of mineral matrix in kerogen pyrolysis: influence on petroleum generation and migration. Am Assoc Pet Geol Bull 1980;64:59–66.
[21] Karabakan A, Yürüm Y. Effect of the mineral matrix in the reactions of oil shales: 1. Pyrolysis reactions of Turkish Göynük and US Green River oil shales. Fuel 1998;77:1303–9.
[22] Cnudde V, Boone MNN. High-resolution X-ray computed tomography in geosciences: a review of the current technology and applications. Earth-Sci Rev 2013;123:1–17. https://doi.org/10.1016/j.earscirev.2013.04.003.
[23] Lin Q, Neethling SJ, Dobson KJ, Courtois L, Lee PD. Quantifying and minimising systematic and random errors in X-ray micro-tomography based volume measurements. Comput Geosci 2015;77:1–7. https://doi.org/10.1016/j.cageo.2014.12.008.
[24] Wildenschild D, Sheppard AP. X-ray imaging and analysis techniques for quantifying pore-scale structure and processes in subsurface porous medium systems. Adv Water Resour 2013;51:217–46. https://doi.org/10.1016/j.advwatres.2012.07.018.
[25] Tiwari P, Deo M, Lin CL, Miller JD. Characterization of oil shale pore structure before and after pyrolysis by using X-ray micro CT. Fuel 2013;107:547–54. https://doi.org/10.1016/j.fuel.2013.01.006.
[26] Saif T, Lin Q, Bijeljic B, Blunt MJ. Microstructural imaging and characterization of oil shale before and after pyrolysis. Fuel 2017;197:562–74.
[27] Saif T, Lin Q, Butcher AR, Bijeljic B, Blunt MJ. Multi-scale multi-dimensional microstructure imaging of oil shale pyrolysis using X-ray micro-tomography, automated ultra-high resolution SEM, MAPS Mineralogy and FIB-SEM. Appl Energy 2017;202:628–47.
[28] Renard F, Cordonnier B, Kobchenko M, Kandula N, Weiss J, Zhu W. Microscale characterization of rupture nucleation unravels precursors to faulting in rocks. Earth Planet Sci Lett 2017;476:69–78.
[29] Figueroa Pilz F, Dowey PJ, Fauchille A, Courtois L, Bay B, Ma L, et al. Synchrotron tomographic quantification of strain and fracture during simulated thermal maturation of an organic-rich shale, UK Kimmeridge Clay. J Geophys Res Solid Earth 2017;122:2553–64.
[30] Panahi H, Meakin P, Renard F, Kobchenko M, Scheibert J, Mazzini A, et al. A 4D synchrotron X-ray-tomography study of the formation of hydrocarbon-migration pathways in heated organic-rich shale. SPE J 2013;18:366–77. https://doi.org/10.2118/162939-PA.
[31] Winick H. Synchrotron radiation sources—a primer vol. 1. World Scientific; 1995.
[32] Lifshin E. X-ray characterization of materials. John Wiley & Sons; 2008.
[33] Landis EN, Keane DT. X-ray microtomography. Mater Charact 2010;61:1305–16.
[34] Saif T, Lin Q, Singh K, Bijeljic B, Blunt MJ. Dynamic imaging of oil shale pyrolysis using synchrotron X-ray micro-tomography. Geophys Res Lett 2016. https://doi.org/10.1002/2016GL069279.
[35] Bay BK, Smith TS, Fyhrie DP, Saad M. Digital volume correlation: three-dimensional strain mapping using X-ray tomography. Exp Mech 1999;39:217–26.
[36] Stampanoni M, Groso A, Isenegger A, Mikuljan G, Chen Q, Bertrand A, et al. Trends in synchrotron-based tomographic imaging: the SLS experience. Dev. X-ray Tomogr. V 2006;vol. 6318. p. 63180M.
[37] Shearing PR, Howard LE, Jørgensen PS, Brandon NP, Harris SJ. Characterization of the 3-dimensional microstructure of a graphite negative electrode from a Li-ion battery. Electrochem Commun 2010;12:374–7.

[38] Meng Q-T, Liu Z-J, Liu R, Sun P-C, Hu F, Zhang J. Comparision on the characteristics of biomarkers of oil shale between Huadian Formatin in Huadian Basin and Green River Formation in Uinta Basin of western United States. J Jilin Univ Sci Ed 2011;41:391–9.
[39] Fife JL, Rappaz M, Pistone M, Celcer T, Mikuljan G, Stampanoni M. Development of a laser-based heating system for in situ synchrotron-based X-ray tomographic microscopy. J Synchrotron Radiat 2012;19:352–8.
[40] Marone F, Stampanoni M. Regridding reconstruction algorithm for real-time tomographic imaging. J Synchrotron Radiat 2012;19:1029–37.
[41] Buades A, Coll B, Morel J-M. Nonlocal image and movie denoising. Int J Comput Vis 2008;76:123–39. https://doi.org/10.1007/s11263-007-0052-1.
[42] Fincham AM, Spedding GR. Low cost, high resolution DPIV for measurement of turbulent fluid flow. Exp Fluids 1997;23:449–62.
[43] Scarano F, Riethmuller ML. Advances in iterative multigrid PIV image processing. Exp Fluids 2000;29:S051–60.
[44] White AJ. A comparison of modelling methods for polydispersed wet-steam flow. Int J Numer Methods Eng 2003;57:819–34.
[45] Blunt MJ. Multiphase flow in permeable media: a pore-scale perspective. Cambridge University Press; 2017.